2010 IEEE International Conference on Robotics and Automation
Anchorage Convention District
May 3-8, 2010, Anchorage, Alaska, USA

OctoMag: An Electromagnetic System for 5-DOF Wireless Micromanipulation

Michael P. Kummer, Jake J. Abbott, Bradley E. Kratochvil, Ruedi Borer, Ali Sengul, and Bradley J. Nelson

Abstract— **We demonstrate five-degree-of-freedom (5-DOF) wireless magnetic control of a fully untethered microrobot (3-DOF position, 2-DOF pointing orientation). The microrobot can move through a large workspace, and is completely unrestrained in the rotation degrees of freedom. We accomplish this level of wireless control with an electromagnetic system that we call OctoMag. OctoMag's unique abilities are due to its utilization of complex nonuniform magnetic fields, which capitalizes on a linear representation of the coupled field contributions of multiple soft-magnetic-core electromagnets acting in concert. OctoMag was primarily designed for the control of intraocular microrobots for delicate retinal procedures, but it also has potential uses in other medical applications or micromanipulation under an optical microscope.**

I. Introduction

One approach to the wireless control of microrobots is through externally applied magnetic fields. These untethered devices can navigate in bodily fluids to enable a number of new minimally invasive therapeutic and diagnostic medical procedures. We are particularly interested in intraocular microrobots, which have the potential to be used in ophthalmic procedures such as drug delivery and remote sensing [1]. With the goal of enabling less invasive and safer retinal surgery, as well as providing an increased level of dexterity desired by clinicians, we embarked on the design of a system for magnetic manipulation of a fully untethered dexterous microrobotic device inside the eye. A magnetic device is fundamentally force controlled, with localization required for closed-loop position control, as opposed to manual surgery and existing robotic tools [2]–[4], which are fundamentally position controlled with force sensing or visual feedback of tissue interaction required for closed-loop force control. This makes a magnetic tool a safer device for interacting with the retina: we can impose limits on the system to make irreparable retinal damage impossible, even in the event of patient movement or system failure. Ophthalmic procedures are also unique among minimally invasive medical procedures in that they provide a direct line of sight for visual feedback, making closed-loop position control of intraocular microrobots possible.

The result of our design is an electromagnetic system that we call OctoMag. The prototype system is shown in Fig. 1, and a concept image showing how OctoMag would be used for control of intraocular microrobots is shown in Fig. 2. OctoMag enables five-degree-of-freedom (5-DOF) wireless magnetic control of a fully untethered microrobot (3-DOF position, 2-DOF pointing orientation). The microrobot can move through a large workspace and is completely unrestrained in the rotation degrees of freedom, which has not been demonstrated previously. Whereas magnetic manipulation has typically relied on orthogonal electromagnetic arrangements generating uniform fields and so-called uniform-gradient fields, which are simple in terms of modeling and control, OctoMag's level of wireless control is due to its utilization of complex nonuniform magnetic fields.

Fig. 1. The OctoMag prototype contains eight 210-mm-long by 62-mm-diameter electromagnets. The gap between two opposing electromagnets on the lower set is 130 mm. The inset is the side-camera view, and shows a 2-mm-long microrobot of the type described in [5].

The original goal of the OctoMag project was 5-DOF wireless manipulation using stationary soft-magnetic-core electromagnets configured to respect the geometry of the human head, neck, and shoulders for the control of intraocular microrobots. We began our open-ended design problem by first solving the control-system problem: Given an arbitrary number of stationary electromagnets in an arbitrary configuration, what is a viable control system for 5-DOF control of magnetic microrobots? Using the developed control system, we considered the performance of the resulting system to optimize the design of the electromagnet configuration.

There is a large body of prior work discussing wireless manipulation with magnetic fields, using a wide variety of techniques. A significant portion of that work is aimed at medical applications [6]. Some of the earliest systems were designed to pull a magnetic seed through brain tissue using incremental pulses [7], but were not capable of stable real-

This work is supported by the NCCR Co-Me of the Swiss National Science Foundation.

The authors are with the Institute of Robotics and Intelligent Systems, ETH Zurich, 8092 Zurich, Switzerland. e-mail: bnelson@ethz.ch. J. J. Abbott is now with the Department of Mechanical Engineering, University of Utah, Salt Lake City, UT, 84112 USA.

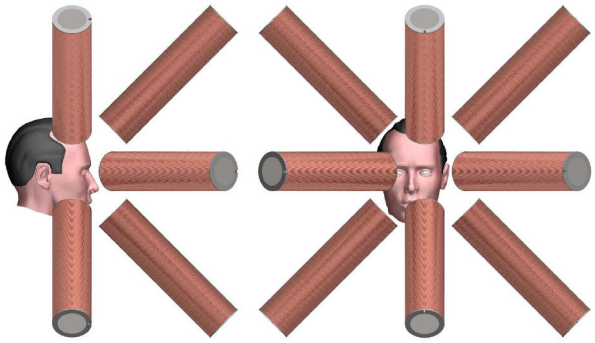

Fig. 2. Concept image of the OctoMag electromagnetic system for the control of intraocular microrobots. An eyeball is at the center of the system's workspace. The electromagnet arrangement accommodates the geometry of the head, neck, and shoulders. The OctoMag is designed for a camera to fit down the central axis to image the microrobot in the eye. Homothetically increasing the size of the prototype system to accommodate a human head will require more powerful current amplifiers to generate the same magnetic field strength. In addition, because the strength of the field gradients attenuates by the same factor by which the system is scaled, the optimal balance of magnetic field and field gradients for a given manipulation task is likely to change compared to the prototype system.

time control of untethered devices. There is currently one wireless magnetic system in clinical use: the Stereotaxis Niobe Magnetic Navigation System, which uses two massive permanent magnets to steer magnetically tipped catheters in the cardiovascular system. It has been shown that the coils of a clinical magnetic resonance imaging (MRI) system can be used to control untethered magnetic beads in 3-DOF [8]. A variety of swimming magnetic microrobots have been developed, nominally for biomedical applications, including helical microrobots inspired by the propulsion of bacterial flagella [9], [10] and microrobots propelled by elastic-tails [11] and chains of paramagnetic beads [12] that are inspired by the propulsion of eukaryotic flagella. Researchers have developed a variety of wireless magnetic microrobots that demonstrate impressive performance on planar surfaces, but that rely on the planar surface to support the microrobot's weight. These include pulling laterally on the microrobot with magnetic field gradients [5], exciting resonance in the microrobot's structure [13], and creating rocking motions of the microrobot that results in net lateral movement [14], [15]. A number of groups have created electromagnetic systems for 3-DOF manipulation of small magnetic particles in fluid under a microscope [16], and others have demonstrated 3-DOF manipulation of a microrobot levitated in air [17]. A few magnetic levitation systems have demonstrated 6-DOF controlled movement, but it has always been over a very restricted workspace, particularly in the rotation degrees of freedom [18]–[20].

II. Control with Stationary Electromagnets

Our goal is to perform 5-DOF wireless control of a magnetic microrobot with respect to a stationary world frame of reference. We assume that the microrobot to be controlled is a magnetized body described by a magnetic moment $\mathbf{M}$ in units $\mathrm{A}\cdot\mathrm{m}^2$. With a permanent magnet, the magnetic moment $\mathbf{M}$ is assumed to have a constant magnitude and be rigidly connected to the frame of the body. With a soft-magnetic body, the magnetic moment is dependent on the applied field and cannot be assumed to be rigidly attached to the body. That is, the magnetic moment can rotate with respect to the body and its magnitude can vary greatly with changes in the applied field. In prior work, we have generated accurate models for the field-dependent magnetic moment of axially symmetric bodies [21], which includes ellipsoids and spheres, as well as assembled-MEMS structures [22] like those used in this paper.

The torque on the magnet, in units $\mathrm{N}\cdot\mathrm{m}$, is expressed as

$$\mathbf{T} = \mathbf{M} \times \mathbf{B} \tag{1}$$

where $\mathbf{B}$ is the value of the applied magnetic field's flux density at the location of $\mathbf{M}$ in units T [23]. The torque tends to align the magnetic moment with the applied field. In the case of soft-magnetic bodies, the torque tends to align the longest axis of the body (referred to as the easy axis) with the field. Assuming uniform magnetization throughout the body—a valid assumption for small elliptical shapes—it is difficult to control torque about the axis of $\mathbf{M}$ using the simple model in (1), which is the reason why our goal is to achieve 5-DOF control rather than 6-DOF control. In soft-magnetic bodies, this means that we are unable to perform rotations about the long axis of the body. The force on the magnetic moment, in units N, is expressed as $\mathbf{F} = (\mathbf{M}\cdot\nabla)\,\mathbf{B}$. Since there is no electric current flowing through the region occupied by the body, Maxwell's equations provide the constraint $\nabla\times\mathbf{B} = \mathbf{0}$, allowing us to express the force in a more intuitive form:

$$\mathbf{F} = \begin{bmatrix} \dfrac{\partial \mathbf{B}}{\partial x} & \dfrac{\partial \mathbf{B}}{\partial y} & \dfrac{\partial \mathbf{B}}{\partial z} \end{bmatrix}^T \mathbf{M} \tag{2}$$

Note that we can also describe the applied magnetic field by $\mathbf{H}$ in $\mathrm{A/m}$, with $\mathbf{B} = \mu_0\mathbf{H}$ and $\mu_0 = 4\pi\times 10^{-7}\ \mathrm{T}\cdot\mathrm{m/A}$.

Within a given static arrangement of electromagnets, each electromagnet creates a magnetic field throughout the workspace that can be precomputed. At any given point in the workspace $\mathbf{P}$, we can express the magnetic field due to a given electromagnet by the vector $\mathbf{B}_e(\mathbf{P})$, whose magnitude varies linearly with the current through the electromagnet, and as such can be described as a unit-current vector in units $\mathrm{T/A}$ multiplied by a scalar current value in units A:

$$\mathbf{B}_e(\mathbf{P}) = \tilde{\mathbf{B}}_e(\mathbf{P}) i_e \tag{3}$$

The subscript e represents the contribution due to the e^{th} electromagnet. The field $\mathbf{B}_e(\mathbf{P})$ is the field due to the current flowing through electromagnet e and due to the soft-magnetic cores of every electromagnet. With air-core electromagnets, the individual field contributions are decoupled, and the fields can be individually precomputed and then linearly superimposed. This in not the case with soft-magnetic-core electromagnets. However, if we assume an ideal soft-magnetic material with negligible hysteresis, and we operate the system with the cores in their linear magnetization region, we can still assume that the field contributions of the individual currents (each of which affect the magnetization

of every core) superimpose linearly. Thus, if we precompute the field contribution of a given electromagnet *in situ*, we can assume that the magnetic field at a point in the workspace is the sum of the contributions of the individual currents:

$$\mathbf{B}(\mathbf{P}) = \sum_{e=1}^{n} \mathbf{B}_e(\mathbf{P}) = \sum_{e=1}^{n} \tilde{\mathbf{B}}_e(\mathbf{P}) i_e \tag{4}$$

This assumption is clearly also valid for air-core electromagnets. This linear summation of fields can be expressed as:

$$\mathbf{B}(\mathbf{P}) = \begin{bmatrix} \tilde{\mathbf{B}}_1(\mathbf{P}) & \cdots & \tilde{\mathbf{B}}_n(\mathbf{P}) \end{bmatrix} \begin{bmatrix} i_1 \\ \vdots \\ i_n \end{bmatrix} = \mathcal{B}(\mathbf{P}) I \tag{5}$$

The $3 \times n$ $\mathcal{B}(\mathbf{P})$ matrix is known at each point in the workspace and can be calculated online, or calculated offline and then interpolated. It is also possible to express the derivative of the field in a given direction in a specific frame, for example the x direction, as the contributions from each of the currents:

$$\frac{\partial \mathbf{B}(\mathbf{P})}{\partial x} = \begin{bmatrix} \frac{\partial \tilde{\mathbf{B}}_1(\mathbf{P})}{\partial x} & \cdots & \frac{\partial \tilde{\mathbf{B}}_n(\mathbf{P})}{\partial x} \end{bmatrix} \begin{bmatrix} i_1 \\ \vdots \\ i_n \end{bmatrix} = \mathcal{B}_x(\mathbf{P}) I \tag{6}$$

In the case of a microrobot moving through fluid, where the microrobot can align with the applied field unimpeded, we can simply control the magnetic field to the desired orientation, to which the microrobot will naturally align, and then explicitly control the force on the microrobot:

$$\begin{bmatrix} \mathbf{B} \\ \mathbf{F} \end{bmatrix} = \begin{bmatrix} \mathcal{B}(\mathbf{P}) \\ \mathbf{M}^T \mathcal{B}_x(\mathbf{P}) \\ \mathbf{M}^T \mathcal{B}_y(\mathbf{P}) \\ \mathbf{M}^T \mathcal{B}_z(\mathbf{P}) \end{bmatrix} \begin{bmatrix} i_1 \\ \vdots \\ i_n \end{bmatrix} = \mathcal{A}(\mathbf{M}, \mathbf{P}) I \tag{7}$$

That is, for each microrobot pose, the n electromagnet currents are mapped to a field and force through a $6 \times n$ actuation matrix $\mathcal{A}(\mathbf{M}, \mathbf{P})$. For a desired field/force vector, the choice of currents that gets us closest to the desired field/force value can be found using the pseudoinverse:

$$I = \mathcal{A}(\mathbf{M}, \mathbf{P})^{\dagger} \begin{bmatrix} \mathbf{B}_{\text{des}} \\ \mathbf{F}_{\text{des}} \end{bmatrix} \tag{8}$$

Full 5-DOF control requires a rank-6 actuation matrix $\mathcal{A}$. If there are multiple solutions to achieve the desired field/force, the pseudoinverse finds the solution that minimizes the 2-norm of the current vector, which is desirable for the minimization of both energy consuption and heat generation. Note that the use of (8) requires knowledge of the microrobot's pose and magnetic moment. If we ensure that the direction of $\mathbf{B}$ does not change too rapidly, it is reasonable to assume that $\mathbf{M}$ is always aligned with $\mathbf{B}$, which means that we need not explicitly measure the microrobot's full pose, but rather, only estimate the magnitude of $\mathbf{M}$ and measure the microrobot's position $\mathbf{P}$. In addition, if we can generate a magnetic field that does not vary greatly across the workspace, it may be reasonable to assume that the microrobot is always located at $\mathbf{P} = \mathbf{0}$ for purposes of control, eliminating the need for any localization of the microrobot.

There are a number of potential methods to generate the unit-current field maps that are required for the proposed control system. We may either explicitly measure the magnetic field of the final system at a grid of points or compute the field values at the grid of points using FEM models, and then use trilinear interpolation during run time. To generate the unit-current gradient maps using either method, we may either explicitly measure/model the gradient at the grid of points, or numerically differentiate the field data. In this paper, we choose to fit a simple analytical model—the point-dipole model—to field data obtained from an FEM model of the final system for each of the unit-current contributions. The analytical field model also has a simple analytical derivative. These analytical models are used to build the unit-current field and gradient maps during run time.

Throughout this work, we use a constant $|\mathbf{B}| = 15\ \text{mT}$ at the location of the microrobot: a value chosen after pilot testing because it results in low peak currents in the electromagnets during typical operation. Keeping $|\mathbf{B}|$ constant keeps the control-system equations linear and enables (8) to be computed in one iteration, but it is suboptimal. Allowing $|\mathbf{B}|$ to vary would result in somewhat better performance, but at the added computation cost of optimization in real time. This is left as a topic for future work.

Traditional wisdom is that developing linear control systems requires air-core electromagnets, whose individual fields linearly superimpose. However, soft-magnetic cores are desirable here because they provide an approximately $20\times$ increase in magnetic-field strength compared to air-core electromagnets. Computing the linear contributions of multiple electromagnets that have high-performance soft-magnetic cores *in situ* is the concept that ultimately leads to the system developed in this paper.

III. Design of the Electromagnet Configuration

Once equipped with a general control system using n electromagnets, it is possible to use this controller in the design of the electromagnet configuration. The singular values of the actuation matrix give information about the condition of the workspace (i.e., points and configurations where we lose control authority in certain directions). Since the units for flux density and force are not the same, it is difficult to characterize the system with some condition number based on singular values [24]. When we consider the practical requirements of the control system, it is more important to accurately control force than field. Accurate force control will be needed to levitate the microrobot against its own weight in gravity, or to push on an object with a specific force. Field, on the other hand, is only needed to rotate the microrobot, and a low field applied in the correct direction will ultimately result in the correct control effort, with only the rise time of the controller being affected. With this design specification in mind, we consider a modified actuation matrix where the field equations are assumed to be

attenuated from their true value by some factor $\alpha \ll 1$:

$$\begin{bmatrix} \alpha\mathbf{B} \\ \mathbf{F} \end{bmatrix} = \begin{bmatrix} \alpha\mathcal{B}(\mathbf{P}) \\ \mathbf{M}^T\mathcal{B}_x(\mathbf{P}) \\ \mathbf{M}^T\mathcal{B}_y(\mathbf{P}) \\ \mathbf{M}^T\mathcal{B}_z(\mathbf{P}) \end{bmatrix} \begin{bmatrix} i_1 \\ \vdots \\ i_n \end{bmatrix} = \mathcal{A}_m(\mathbf{M},\mathbf{P})I \quad (9)$$

For the singular value decomposition of $\mathcal{A}_m = U\Sigma V^T$ the singular values and output singular vectors of $\mathcal{A}_m$ decouple into pure force and pure field directions, as $\alpha \to 0$. σ_4, σ_5, and σ_6 become small due to α, and the columns U_4, U_5, and U_6 become almost pure field directions. This makes σ_1, σ_2, and σ_3 correspond to almost pure force directions, and we can use the ratio σ_3/σ_1 as a force condition number for our system, which is close to 1 if the system has isotropic force control authority in every direction of the workspace. Keeping $\alpha > 0$ and ensuring that $\sigma_6 \neq 0$ will ensure that the generation of field, and thus microrobot orientation, is also possible in every desired direction. The force condition number may not be the best metric to judge our system's performance, since a system that has force generation that is equally poor in each direction will return a good force condition number. Consequently, we use σ_3, which is a measure of force generation in the worst-case direction, as our performance metric during design. Our goal is to have sufficient force generation capability throughout the workspace, regardless of microrobot orientation, such that we never lose control authority of the microrobot.

To design an electromagnet configuration to achieve the desired goals, we begin with some design constraints on the degrees of freedom allowed during optimization (see Fig. 3): We consider two sets of m electromagnets (with $n = 2m$), which we will refer to as the *upper* and *lower* sets, although our goal is a system that has no preferential directions of control, and consequently, no distinction between up and down. Each electromagnet is modeled as a unit-strength point-dipole [23] pointing at the common center of the workspace and located at a distance d from the center. The upper and lower sets are organized around a common axis of rotation, and they are equally spaced around the common axis. The angle between the electromagnets in the upper set and the common axis is defined as ϕ_{upper}, and ϕ_{lower} is defined analogously. Finally, the lower set is allowed to rotate with respect to the upper set by θ.

During optimization, we set $d = 65$ mm (our size requirement for use in trials on small mammals, but arbitrary for the design optimization) and $m = \{3, 4\}$ (one at a time) as constants. We allow the other parameters to vary in the bounded sets $\phi_{\text{upper}} \in [0, 90°]$, $\phi_{\text{lower}} \in [0, 180°]$, and $\theta \in [0, 60°]$. For a given configuration, we considered the point at the common center of the electromagnets, as well as 17 regularly spaced points that define a hemisphere of radius 10 mm (roughly the radius of a human eye). At each of these points, we considered a unit-strength dipole moment (the microrobot) at 26 cardinal orientations. The optimization metric for the electromagnet configuration is the lowest (worst case) σ_3 out of the 468 microrobot poses, and the optimization routine (MATLAB's *fmincon*) attempts

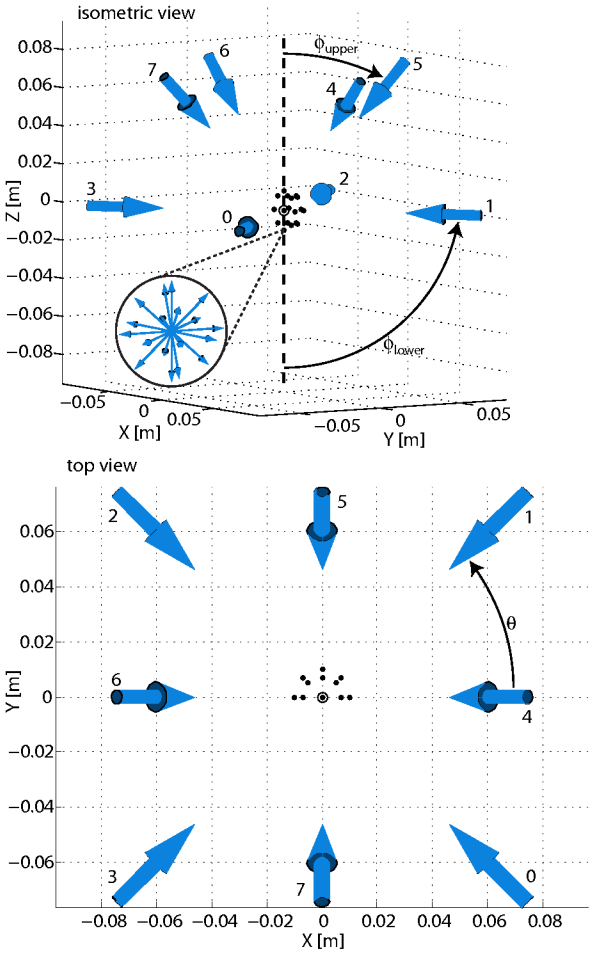

Fig. 3. Optimization of the electromagnet configuration. The upper and lower sets each contain m equally spaced dipoles at an angle ϕ_{upper} and ϕ_{lower} from the common axis, respectively. $m = 4$ shown. The dipoles all point at a common center, indicated by a circle. The lower set is rotated with respect to the upper set by θ. The 18 microrobot points considered span a hemisphere; each point is indicated by a dot. At each point, 26 microrobot orientations are considered, shown in the inset. The coil numbering is used for visualization purpose.

to maximize this metric. The parameters are allowed to vary without consideration of potential collisions between the electromagnets. N.B. that the commonly used configuration of six electromagnets arranged orthogonally, pointing at a common center (e.g. three orthogonal coil pairs) is a special case allowed by this optimization ($m = 3$, $\theta = 60°$, $\phi_{\text{upper}} = 45°$, $\phi_{\text{lower}} = 45°$).

The result of the presented optimization routine is the OctoMag configuration shown in Figs. 1–3. For both permanent-magnet and soft-magnetic microrobots, a configuration with $m = 4$, $\theta = 45°$, $\phi_{\text{upper}} \approx 45°$, and $\phi_{\text{lower}} \approx 90°$ resulted in the best performance. The performance of the system is insensitive to small changes in these nominal values. We found nearly an order of magnitude improvement in the worst-case microrobot pose when we increased from $m = 3$ to $m = 4$ (i.e. from 6 to 8 electromagnets). Probably the most striking feature of the OctoMag configuration is its lack of symmetry. Intuition might lead one to believe that

electromagnets must uniformly surround the workspace in order to create an isotropic behavior, but this is not the case. With the hemispherical OctoMag configuration, we can push downward, and pull upward and sideways, and we can do it while maintaining any microrobot orientation.

IV. System Implementation

Each electromagnet consists of a coil that has dimensions $d_i = 44\,\mathrm{mm}$, $d_o = 63.2\,\mathrm{mm}$ and $l = 210\,\mathrm{mm}$, where d_i, d_o, and l are inner diameter, outer diameter, and length, respectively. The coil carries 712 wraps of 1.6-mm diameter, insulated copper wire. The electromagnet cores are made of VACOFLUX 50, which is a CoFe alloy from VACUUMSCHMELZE. Its saturation magnetization is on the order of $2.3\,\mathrm{T}$, the coercivity is $0.11\,\mathrm{mT}$, and the maximum permeability is $4500\,\mathrm{H/m}$. The core has diameter $42\,\mathrm{mm}$ and length $210\,\mathrm{mm}$. The maximum dimension of the electromagnet tip is limited through geometry. Taking this spatial limitation into consideration, the ratio of core radius to core length was chosen such that a current density of $\sim 700\,\mathrm{A/cm^2}$ would suffice to saturate the core while providing the required magnetic field strength. The electromagnet has an inductance of $89\,\mathrm{mH}$ and a resistance of $1.3\,\Omega$.

The power supply for the system is an SM 70-90 by Delta Elektronica BV. This supply is capable of providing $6\,\mathrm{kW}$ to the system, and enables all eight channels to be simultaneously driven at $20\,\mathrm{A}$. To reduce the power consumption of the electronics, the current for the electromagnetic coils is sourced through custom-designed switched amplifiers. The switching frequency of these amplifiers is $150\,\mathrm{kHz}$, which is well above the frequency that would influence control of the microrobot. The switched amplifiers are controlled through two Sensoray 626 DAC cards with 14-bit resolution.

To prevent the temperature in the coils from reaching a critical stage, a cooling system consisting of copper tubing that surrounds each coil has been implemented. While running cooling water through the tubing, temperatures have not exceeded $45\,^\circ\mathrm{C}$ with prolonged application of the maximum current the system is capable of exerting (which rarely occurs in practice).

Two stationary camera assemblies provide visual feedback from the top and side. The cameras are Basler A602f 100 fps monochrome CMOS firewire cameras. The cameras are each fitted with an Edmund Optics VZM 200i $2\times$ zoom lens with a working distance of $90\,\mathrm{mm}$, a depth-of-field of $1.5\,\mathrm{mm}$, and a frame size of 640×480 pixels with an effective pixel size of $19.89\,\mu\mathrm{m}$. Each camera assembly is mounted on a Thorlabs DT25/M translation stage, which is used for focusing. Position feedback is achieved with visual processing using the OpenCV library. The simplified experimental environment—a transparent plastic vial—enables successful tracking through the use of adaptive thresholding and morphological operators such as erosion and dilation. The tracking precision is primarily limited by the resolution of the cameras and optics as discussed in Section VI. The entire system is controlled through C++ by a single computer with an Intel Core 2 Duo $2.6\,\mathrm{GHz}$ processor running Ubuntu Linux.

TABLE I

Max force on large CoNi microrobot for various orientations.

Field Orientation	$\mathbf{F}_{\text{up}}$ (μN)	$\mathbf{F}_{\text{down}}$ (μN)	$\mathbf{F}_{\text{lat,x}}$ (μN)	$\mathbf{F}_{\text{lat,y}}$ (μN)	$\mathbf{F}_{\text{lat,xy}}$ (μN)
z	42	26	25	27	28
$-z$	66	42	36	42	44
x	43	43	72	62	79
xy	55	55	84	61	50

TABLE II

Max force on small Ni microrobot for various orientations.

Field Orientation	$\mathbf{F}_{\text{up}}$ (μN)	$\mathbf{F}_{\text{down}}$ (μN)	$\mathbf{F}_{\text{lat,x}}$ (μN)	$\mathbf{F}_{\text{lat,y}}$ (μN)	$\mathbf{F}_{\text{lat,xy}}$ (μN)
z	2.1	1.3	1.1	1.3	1.4
$-z$	3.3	2.1	1.7	2.0	2.2
x	2.2	2.2	3.6	3.1	3.9
xy	2.7	2.7	4.1	3.0	2.5

V. Force Generation

We are interested in quantifying the maximum force that can be developed with a microrobot, which is a function of the size and geometry of the microrobot and the coil setup. Throughout this paper we consider two assembled-MEMS microrobots of the type discussed in [5]. The microrobots are assembled from two electroplated, planar, nearly elliptical pieces, resulting from the intersection of two circles with their centers at a distance a apart. The dimensions are $a_{\text{CoNi}} = 1.5\,\mathrm{mm}$ and $R_{\text{CoNi}} = 1.25\,\mathrm{mm}$ with a plated thickness of $50\,\mu\mathrm{m}$ for the larger CoNi microrobot, and $a_{\text{Ni}} = 375\,\mu\mathrm{m}$ and $R_{\text{Ni}} = 312.5\,\mu\mathrm{m}$ with a plated thickness of $40\,\mu\mathrm{m}$ for the smaller Ni microrobot, with R denoting circle radius. The volume of the microrobots are respectively $1.35 \times 10^{-10}\,\mathrm{m^3}$ and $6.60 \times 10^{-12}\,\mathrm{m^3}$. With the density of CoNi and Ni being $8900\,\mathrm{kg/m^3}$, their weights are $1.18 \times 10^{-5}\,\mathrm{N}$ and $5.76 \times 10^{-7}\,\mathrm{N}$. For both microrobots, and for $|\mathbf{B}| = 15\,\mathrm{mT}$, the maximum magnetic forces that OctoMag can develop in a variety of microrobot configurations are given in Tables I and II. The values all assume a $15\,\mathrm{A}$ saturation of the current amplifiers. They also assume the microrobot is at the center of the workspace, but the values are representative of the maximum forces throughout the workspace. Because setting $|\mathbf{B}| = 15\,\mathrm{mT}$ is a suboptimal choice made to linearize the controller, the values given in Tables I and II represent a lower bound on the true maximum force values.

Magnetic force is proportional to volume, if the geometry is held constant. Because the microrobot's weight is also proportional to volume, the ability to levitate a microrobot is unchanged with the microrobot's size. However, because fluid-drag effects are proportional to surface area, we see a decrease in maximum velocity as we reduce the size of the microrobot. It is also worth noting that the fluid environment provides a buoyancy force approximately %14 of the weight.

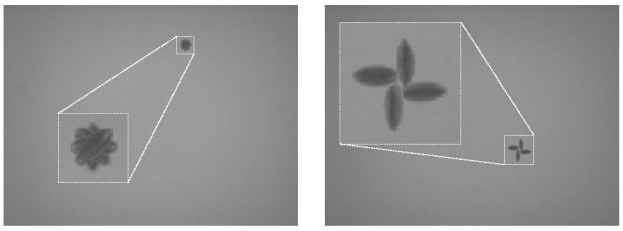

Fig. 4. Demonstration of rotation control. Both time-lapse image sequences show a single 500-µm-long microrobot in the $z = 0$ plane (viewed from above). The left image sequence demonstrates rotation of the microrobot in place at an arbitrary location in space by relying on pure open-loop control. The right image sequence demonstrates rotation of the microrobot about a remote center at an arbitrary location using closed-loop control. Average trajectory-completion time: 5.1 s.

VI. Experimental Demonstration

Earnshaw's theorem tells us that there can be no stable static equilibria using ferromagnetism. That is, to maintain a stable position of the microrobot, we must use feedback control. However, once we have implemented gravity compensation, we empirically find that the drift of the microrobot in a static field is quite slow. For various microrobot orientations, the worst drift at the center of the workspace in a static field is 150 µm/s for the CoNi microrobot and 50 µm/s for the smaller Ni microrobot. At the boundaries of the workspace these values increase to 720 µm/s and 140 µm/s, respectively. Using the microrobot's position for field generation, the drifts at the workspace boundaries reduce to 550 µm/s and 60 µm/s for the CoNi and Ni microrobot, respectively. We see that if we scale the robot down, the effect of drift is reduced—since magnetic forces are proportional to volume, and viscous-drag forces are proportional to surface area—and the behavior and controllability of the microrobot improves. We find that the human operator can regulate the position quite well using a 3Dconnexion SpaceExplorer with only visual feedback, although not with the level of precision as when using the computer-vision tracker for closed-loop control described below.

We also find that the unintended forces that cause drift are smaller than frictional forces when the microrobot is touching a surface. Even the large microrobot resting on a glass surface exhibits no drift in a static field. Along with the small orientation errors incurred when using no position feedback, this indicates that OctoMag has the potential to be used without position feedback.

Since the microrobot can be moved from one location to another in a holonomic fashion, closed-loop control of the microrobot is handled by a simple proportional-derivative controller with tracked position from both cameras. Currently no closed-loop orientation control is implemented, but we find that the error between the robots intended orientation and the actual can be effectively controlled with open-loop control.

To gauge the precision of the system under closed-loop control, the CoNi microrobot was visually servoed to a location in the center of the workspace, and over a period of 13.3 s, the robot's position as returned by the tracker had

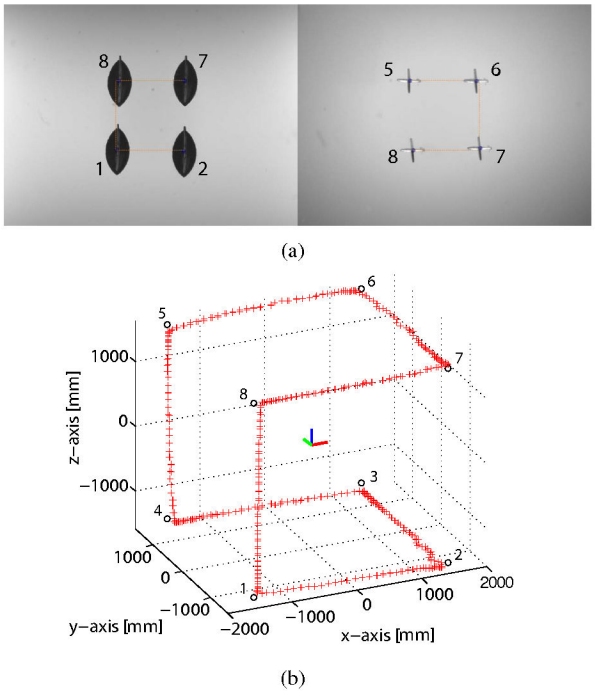

Fig. 5. Demonstration of automated position control. Both composite images (a) show a 2-mm-long microrobot aligned with the Z axis (vertical). The left image demonstrates movement in the $y = -1.5$ mm plane (viewed from the side). The right image demonstrates movement in the $z = 1.5$ mm plane (viewed from above). The microrobot was moved along the edges of a cube as displayed in the isometric graph (b). Black ○ indicate waypoints and red + indicate tracker data. Average trajectory-completion time: 8.2 s.

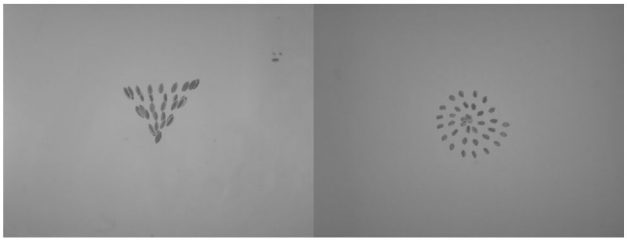

Fig. 6. Demonstration of automated pose control. Both time-lapse image sequences show a 500-µm-long microrobot following a spiral trajectory keeping its orientation constantly pointing at the vertex of the spiral. The left image shows a side view, and the right image shows a top view. Average trajectory-completion time: 33.4 s.

standard deviations of 6.313, 4.757, 8.951 µm along the x, y, and z axes, respectively, and a maximum cartesian deviation of 29.77 µm.

To further demonstrate the performance capabilities of OctoMag under open- and closed-loop control, Figs. 4–6 show a few automated and teleoperated trajectories of the device. The system exhibits similar performance for a wide array of different trajectories as well as a robot orientations.

VII. Discussion

This work focuses on the use of OctoMag for the control of fully untethered microrobots. OctoMag is also capable of applying controlled magnetic forces and torques in 5-DOF to tethered devices, such as magnetically tipped catheters and guidewires. OctoMag also has potential uses that go

beyond medical applications. For example, the OctoMag configuration could be scaled down and used to control microdevices under a light microscope. Since the workspace is designed to be isotropic, OctoMag can be operated upside down or on its side. OctoMag can also be used to control magnetic microrobots that were originally designed to be controlled with uniform magnetic fields. Consider, for example, microscopic helical swimmers designed to be controlled by a rotating uniform magnetic field [10]. With OctoMag, we can set the field to any desired value and simply set $\mathbf{F} = \mathbf{0}$ to effectively generate a uniform field. However, if we apply magnetic force to the microrobot as we rotate it, the magnetic force will sum with the fluidic propulsive force, resulting in higher manipulation forces. Considering the desirable propulsive properties of helical magnetic swimmers as they are scaled down [25], this may actually result in larger useful pushing force than is possible with the type of microrobots shown in this paper.

In order to use the OctoMag for the control of intraocular microrobots, we must still determine for which vitreoretinal procedures an untethered microrobot is appropriate. Microrobots can clearly be used for remote sensing applications, as well as for targeted delivery of small quantities of concentrated drug. There are two potential drawbacks of magnetic microrobots: their limited ability to apply large forces, and their limited ability to carry large payloads.

VIII. Conclusion

We presented five-degree-of-freedom (5-DOF) wireless magnetic control of a fully untethered microrobot, using an electromagnetic system that we call OctoMag. The system provides precise positioning under closed-loop control with computer vision, but can also be used without any visual tracking, relying only on visual feedback to the human operator during direct teleoperation. OctoMag was designed for the control of intraocular microrobots for minimally invasive retinal therapy and diagnosis, but it also has potential for use as a wireless micromanipulation system under a light microscope.

Acknowledgment

The authors would like to thank Dr. Karl Vollmers for many fruitful discussions in the early stages of the OctoMag project. The authors would like to thank Justus Garweg, M.D., from the Swiss Eye Institute in Bern, for his guidance on vitreoretinal applications for untethered microrobots.

References

[1] O. Ergeneman, G. Dogangil, M. P. Kummer, J. J. Abbott, M. K. Nazeeruddin, and B. J. Nelson, "A magnetically controlled wireless optical oxygen sensor for intraocular measurements," *IEEE Sensors J.*, vol. 8, no. 1, pp. 29–37, 2008.

[2] C. N. Riviere, W. T. Ang, and P. K. Khosla, "Toward active tremor canceling in handheld microsurgical instruments," *IEEE Trans. Robotics and Automation*, vol. 19, no. 5, pp. 793–800, 2003.

[3] B. Mitchell, J. Koo, I. Iorcachita, P. Kazanzides, A. Kapoor, J. Handa, G. Hager, and R. Taylor, "Development and application of a new steady-hand manipulator for retinal surgery," in *Proc. IEEE Int. Conf. Robotics and Automation*, 2007, pp. 623–629.

[4] W. Wei, R. E. Goldman, H. F. Fine, S. Chang, and N. Simaan, "Performance evaluation for multi-arm manipulation of hollow suspended organs," *IEEE Trans. Robotics*, vol. 25, no. 1, pp. 147–157, 2009.

[5] K. B. Yesin, K. Vollmers, and B. J. Nelson, "Modeling and control of untethered biomicrorobots in a fluidic environment using electromagnetic fields," *Int. J. Robotics Research*, vol. 25, no. 5–6, pp. 527–536, 2006.

[6] G. T. Gillies, R. C. Ritter, W. C. Broaddus, M. S. Grady, M. A. Howard III, and R. G. McNeil, "Magnetic manipulation instrumentation for medical physics research," *Review of Scientific Instruments*, vol. 65, no. 3, pp. 533–562, 1994.

[7] D. C. Meeker, E. H. Maslen, R. C. Ritter, and F. M. Creighton, "Optimal realization of arbitrary forces in a magnetic stereotaxis system," *IEEE Trans. Magnetics*, vol. 32, no. 2, pp. 320–328, 1996.

[8] S. Martel, J.-B. Mathieu, O. Felfoul, A. Chanu, E. Aboussouan, S. Tamaz, and P. Pouponneau, "Automatic navigation of an untethered device in the artery of a living animal using a conventional clinical magnetic resonance imaging system," *Applied Physics Lett.*, vol. 90, no. 11, pp. 114 105(1–3), 2007.

[9] K. Ishiyama, K. I. Arai, M. Sendoh, and A. Yamazaki, "Spiral-type micro-machine for medical applications," *J. Micromechatronics*, vol. 2, no. 1, pp. 77–86, 2003.

[10] L. Zhang, J. J. Abbott, L. X. Dong, B. E. Kratochvil, D. Bell, and B. J. Nelson, "Artificial bacterial flagella: Fabrication and magnetic control," *Applied Physics Lett.*, vol. 94, no. 064107, 2009.

[11] S. Sudo, S. Segawa, and T. Honda, "Magnetic swimming mechanism in a viscous liquid," *J. Intelligent Material Systems and Structures*, vol. 17, pp. 729–736, 2006.

[12] R. Dreyfus, J. Baudry, M. L. Roper, M. Fermigier, H. A. Stone, and J. Bibette, "Microscopic artificial swimmers," *Nature*, vol. 437, no. 6, pp. 862–865, 2005.

[13] K. Vollmers, D. R. Frutiger, B. E. Kratochvil, and B. J. Nelson, "Wireless resonant magnetic microactuator for untethered mobile microrobots," *Applied Physics Lett.*, vol. 92, no. 144103, 2008.

[14] M. Gauthier and E. Piat, "An electromagnetic micromanipulation systems for single-cell manipulation," *J. Micromechatronics*, vol. 2, no. 2, pp. 87–119, 2004.

[15] C. Pawashe, S. Floyd, and M. Sitti, "Modeling and experimental characterization of an untethered magnetic micro-robot," *Int. J. Robotics Research*, vol. 28, no. 4, pp. 1077–1094, 2009.

[16] F. Amblard, B. Yurke, A. Pargellis, and S. Leibler, "A magnetic manipulator for studying local rheology and micromechanical properties of biological systems," *Review of Scientific Instruments*, vol. 67, no. 3, pp. 818–827, 1996.

[17] M. B. Khamesee, N. Kato, Y. Nomura, and T. Nakamura, "Design and control of a microrobotic system using magnetic levitation," *IEEE/ASME Trans. Mechatronics*, vol. 7, no. 1, pp. 1–14, 2002.

[18] S. Verma, W.-J. Kim, and J. Gu, "Six-axis nanopositioning device with precision magnetic levitation technology," *IEEE/ASME Trans. Mechatronics*, vol. 9, no. 2, pp. 384–391, 2004.

[19] Z. Zhang and C.-H. Menq, "Six-axis magnetic levitation and motion control," *IEEE Trans. Robotics*, vol. 23, no. 2, pp. 196–205, 2007.

[20] P. Berkelman, "A novel coil configuration to extend the motion range of lorentz force magnetic levitation devices for haptic interaction," in *Proc. IEEE/RSJ Int. Conf. Intelligent Robots and Systems*, 2007, pp. 2107–2112.

[21] J. J. Abbott, O. Ergeneman, M. P. Kummer, A. M. Hirt, and B. J. Nelson, "Modeling magnetic torque and force for controlled manipulation of soft-magnetic bodies," *IEEE Trans. Robotics*, vol. 23, no. 6, pp. 1247–1252, 2007.

[22] Z. Nagy, O. Ergeneman, J. J. Abbott, M. Hutter, A. M. Hirt, and B. J. Nelson, "Modeling assembled-MEMS microrobots for wireless magnetic control," in *Proc. IEEE Int. Conf. Robotics and Automation*, 2008, pp. 874–879.

[23] E. P. Furlani, *Permanent Magnet and Electromechanical Devices*. San Diego, California: Academic Press, 2001.

[24] K. L. Doty, C. Melchiorri, E. M. Schwartz, and C. Bonivento, "Robot manipulability," *IEEE Trans. Robotics and Automation*, vol. 11, no. 3, pp. 462–468, 1995.

[25] J. J. Abbott, K. E. Peyer, M. Cosentino Lagomarsino, L. Zhang, L. X. Dong, I. K. Kaliakatsos, and B. J. Nelson, "How should microrobots swim?" *Int. J. Robotics Research*, vol. 28, no. 11-12, pp. 1434–1447, 2009.